TITLE:

Fusion reaction of a weakly-bound nucleus with a deformed target

AUTHOR(S):

Choi, Ki-Seok; Kim, K. S.; Cheoun, Myung-Ki; So, W. Y.; Hagino, K.

Fusion reaction of a weakly bound nucleus with a deformed target

Ki-Seok Choi and K. S. Kim
School of Liberal Arts and Science, Korea Aerospace University, Koyang 412-791, Korea

Myung-Ki Cheoun
Department of Physics, Soongsil University, Seoul 156-743, Korea

W. Y. So
Department of Radiological Science, Kangwon National University at Dogye, Samcheok 245-905, Korea

K. Hagino [*]
Department of Physics, Kyoto University, Kyoto 606-8502, Japan

We discuss the role of deformation of the target nucleus in the fusion reaction of the ^{15}C + ^{232}Th system at energies around the Coulomb barrier, in which ^{15}C is a well-known one-neutron halo nucleus. To this end, we construct the potential between ^{15}C and ^{232}Th with the double folding procedure, assuming that the projectile nucleus is composed of the core nucleus, ^{14}C, and a valence neutron. In addition, we also take into account the coupling to the one-neutron transfer process to the ^{14}C + ^{233}Th configuration. We show that such calculation simultaneously reproduces the fusion cross sections for the ^{14}C + ^{232}Th and the ^{15}C + ^{232}Th systems, implying an important role of the transfer coupling in fusion of neutron-rich nuclei.

I. INTRODUCTION

One of the most important discoveries in nuclei near the neutron drip line is the halo phenomenon [1,2]. It is characterized by a spatially extended density distribution, originating from the weakly bound property of neutron-rich nuclei. Starting from ^{11}Li [2], several other halo nuclei have also been observed successively. For example, ^{6}He, ^{14}Be, and ^{17}B are regarded as two-neutron halo nuclei, while ^{11}Be, ^{15}C, and ^{19}C are categorized as one-neutron halo nuclei [3,4]. Recently, heavier halo nuclei, such as ^{19}C [5], ^{22}C [6], ^{31}Ne [7], and ^{37}Mg [8] have also been found at the Radioactive Ion Beam Facility (RIBF) in RIKEN.

Fusion reactions of halo nuclei have attracted lots of attention [9–19]. It is generally known that fusion cross sections at energies around the Coulomb barrier are sensitive to the structure of colliding nuclei [20–24], and it is thus likely that the halo structure significantly affects fusion reactions, in both static and dynamical ways. With the development of radioisotope technology, a large number of experimental data for fusion of halo nuclei have been accumulated. For instance, fusion cross sections for the ^{11}Li + ^{208}Pb [25], ^{6}He + ^{238}U [26], ^{6}He + ^{209}Bi [27,28], ^{11}Be + ^{209}Bi [29], and ^{15}C + ^{232}Th [30] systems have been reported.

Interestingly, it has been reported that fusion cross sections for the ^{6}He + ^{238}U system [26] do not show any significant influence of the halo structure of ^{6}He even though ^{6}He is a well-known halo nucleus. This is in contrast to fusion cross sections for the ^{11}Li + ^{208}Pb [25] system, which show an enhancement with respect to the fusion cross sections for the ^{9}Li + ^{208}Pb system. The ^{6}He + ^{209}Bi system also shows a similar trend as in the ^{11}Li + ^{208}Pb system [28]. In the case of one-neutron halo nuclei, cross sections for the ^{11}Be + ^{209}Bi system are reported to be similar to those for the ^{10}Be + ^{209}Bi system [29]. Origins for this apparent difference among these systems are not yet understood completely, even though the fissile nature of the ^{238}U may play some role.

In this regard, it is interesting to notice that ^{238}U is a well-deformed nucleus while ^{208}Pb and ^{209}Bi are spherical nuclei. The aim of this paper is to investigate the role of deformation of the target nucleus in fusion of a halo nucleus. To this end, we shall discuss the fusion reaction of the ^{15}C + ^{232}Th system. The ^{15}C nucleus is a one-neutron halo nucleus [4], and its structure is much simpler than the structure of the two-neutron halo nuclei ^{11}Li and ^{6}He. The ^{15}C + ^{232}Th system thus provides an ideal opportunity to disentangle the deformation and the halo effects. Moreover, ^{15}C is heavier than ^{11}Li and ^{6}He, and more significant effects of the target deformation can be expected for the ^{15}C + ^{232}Th system as compared to the ^{11}Li, ^{6}He + ^{238}U systems. Notice that the previous calculation for this system used a very simple spectator model and did not take into account the halo structure of ^{15}C [30]. It has yet to be clarified how much the observed fusion enhancement can be accounted for by taking into account the halo structure of ^{15}C.

[*]hagino.kouichi.5m@kyoto-u.ac.jp

TABLE I. The depth V_0, the radius r_0, and the diffuseness a parameters for the deformed Woods-Saxon potential for the ^{14}C $+$ ^{232}Th reaction. Here, the radius parameter r_0 is defined as $R_0 = r_0(A_P^{1/3} + A_T^{1/3})$, where A_P and A_T are the mass numbers of the projectile and the target nuclei, respectively. The resultant barrier height V_b, the barrier position, R_b, and the barrier curvature $\hbar\Omega$ are also shown.

V_0 (MeV)	r_0 (fm)	a (fm)	V_b (MeV)	R_b (fm)	$\hbar\Omega$ (MeV)
68.174	1.231	0.548	60.66	12.22	4.96

The paper is organized as follows. In Sec. II, we first analyze the fusion of the ^{14}C $+$ ^{232}Th system by using a deformed Woods-Saxon potential. In Sec. III, we analyze the fusion of the ^{15}C $+$ ^{232}Th system and discuss the role of the halo structure and the deformation effect. To this end, we construct the potential between ^{15}C and ^{232}Th with the double folding formalism accounting for the halo structure of the ^{15}C nucleus. We finally summarize the paper in Sec. IV

II. FUSION REACTION OF THE ^{14}C $+$ ^{232}Th system

Before we discuss the fusion cross sections for the ^{15}C $+$ ^{232}Th system, we first analyze the ^{14}C $+$ ^{232}Th system. In order to take into account the deformation effect of the target nucleus ^{232}Th, we employ a deformed Woods-Saxon (WS) potential for the relative motion between the target and the projectile nuclei [22,31,32]:

$$V_{^{14}\text{C}-T}(r,\theta) = -\frac{V_0}{1 + \exp\left[\left(r - R_0 - R_T \sum_\lambda \beta_{\lambda T} Y_{\lambda 0}(\theta)\right)/a\right]},$$
(1)

where V_0, R_0, and a are the depth, the radius, and the diffuseness parameters, respectively. R_T and $\beta_{\lambda T}$ are the radius and the deformation parameters of the target nucleus ^{232}Th. The Coulomb potential also has a deformed form given by [22,31]

$$V_C(r,\theta) = \frac{Z_P Z_T e^2}{r} + \frac{3 Z_P Z_T e^2}{5} \frac{R_T^2}{r^3}\left(\beta_{2T} + \frac{2}{7}\sqrt{\frac{5}{\pi}}\beta_{2T}^2\right)Y_{20}(\theta) + \frac{3 Z_P Z_T e^2}{9} \frac{R_T^4}{r^5}\left(\beta_{4T} + \frac{9}{7\sqrt{\pi}}\beta_{2T}^2\right)Y_{40}(\theta),$$
(2)

with the second order in the quadrupole deformation parameter, β_{2T}, and the first order in the hexadecapole deformation parameter, β_{4T}. Z_P and Z_T are the atomic numbers of the projectile and the target nuclei, respectively. Fusion is simulated with the incoming wave boundary condition [22,31]. For simplicity, in this paper we assume that ^{14}C is inert.

The fusion cross sections for the ^{14}C $+$ ^{232}Th system so obtained are presented in Fig. 1. The actual values for the parameters in the WS potential employed in this calculation are given in Table I. We use the same values for the radius and the diffuseness parameters as those of the global type of Akyüz-Winther (AW) potential [33], while we adjust the depth parameter, V_0 to fit the measured fusion cross sections.
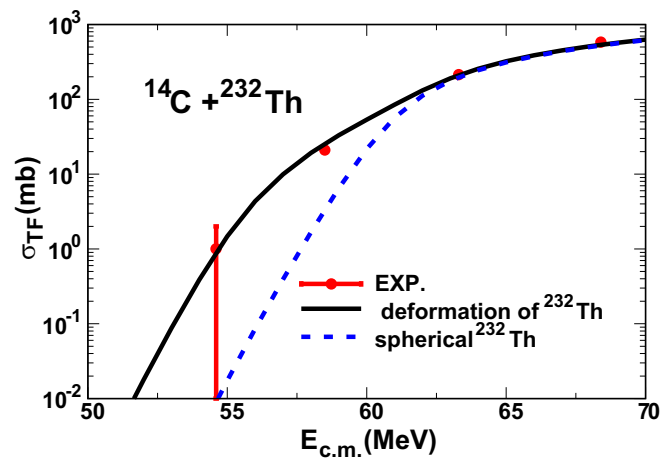

FIG. 1. Fusion cross sections for the ^{14}C $+$ ^{232}Th system. The dashed line denotes cross sections in the absence of the deformation effect of the target nucleus ^{232}Th while the solid line is obtained by taking into account the deformation effect with a deformed Woods-Saxon potential. The experimental data are taken from Ref. [30].

For the deformation parameters, we employ $\beta_{2T} = 0.233$ and $\beta_{4T} = 0.0946$ [34]. In the figure, the blue dashed line shows the cross sections in the absence of the deformation effect, while the black solid line shows the cross sections with the deformation effect. One can clearly see that the enhancement of the fusion cross sections below the Coulomb barrier region can be well accounted for by taking into account the deformation of ^{232}Th. It is apparent that the deformation plays an important role in this system.

III. FUSION REACTION OF THE ^{15}C $+$ ^{232}Th SYSTEM

A. The internuclear potential

Let us now discuss the fusion reaction of the ^{15}C $+$ ^{232}Th system. We first construct the potential between ^{15}C and ^{232}Th taking into account the deformation effect of the target nucleus as well as the halo structure of the projectile. To this end, we employ the double folding approach and construct the potential as

$$V_{^{15}\text{C}-T}(\mathbf{r};\mathbf{r}_d) = \int d\mathbf{r}_p \int d\mathbf{r}_T \rho_p(r_p)\rho_T(\mathbf{r}_T;\mathbf{r}_d) \times V_{NN}(\mathbf{r} - \mathbf{r}_p + \mathbf{r}_T),$$
(3)

where V_{NN} is an effective nucleon-nucleon interaction, while $\rho_p(r_p)$ and $\rho_T(\mathbf{r}_T;\mathbf{r}_d)$ are the density profiles for the projectile and the target nuclei, respectively. Here, the density of the deformed target is defined with respect to the orientation angle, $\mathbf{r}_d$, in the space fixed frame. In this paper, we employ the deformed Woods-Saxon density given by

$$\rho_T(\mathbf{r};\mathbf{r}_d) = \frac{\rho_0}{1 + \exp\left[\left(\frac{r - c(1 + \sum_\lambda \beta_{\lambda T} Y_{\lambda 0}(\theta_{rd}))}{z}\right)\right]},$$
(4)

where θ_{rd} is the angle between $\mathbf{r}$ and $\mathbf{r}_d$, and $\beta_{\lambda T}$ are the deformation parameters. We take $c = 6.851$ fm, $z = 0.518$ fm, and $\rho_0 = 0.162$ fm^{-3} for the ^{232}Th nucleus [35]. For the nucleon-nucleon interaction, V_{NN}, we use the M3Y interaction

[36] given by

$$V_{NN}(r) = -2134\frac{e^{-2.5r}}{2.5r} + 7999\frac{e^{-4r}}{4r} - 275.81\delta(r), \quad (5)$$

where the energy and the length are given in units of MeV and fm, respectively. Notice that this interaction also includes the knock-on exchange effect in the zero-range approximation.

To evaluate the double folding potential, the target density (4) is expanded as

$$\rho_T(\boldsymbol{r};\boldsymbol{r}_d) = \sum_\lambda \rho_{T\lambda}(r)Y_{\lambda 0}(\theta_{rd}) \quad (6)$$

$$= \sum_{\lambda,\mu} \rho_{T\lambda}(r)\sqrt{\frac{4\pi}{2\lambda+1}}Y_{\lambda\mu}(\hat{\boldsymbol{r}})Y_{\lambda\mu}^*(\hat{\boldsymbol{r}}_d). \quad (7)$$

Substituting this into Eq. (3), one obtains the potential in the form of

$$V_{^{15}\mathrm{C}-T}(\boldsymbol{r};\boldsymbol{r}_{\mathrm{def}}) = \sum_{\lambda,\mu} V_\lambda(r)\sqrt{\frac{4\pi}{2\lambda+1}}Y_{\lambda\mu}(\hat{\boldsymbol{r}})Y_{\lambda\mu}^*(\hat{\boldsymbol{r}}_d), \quad (8)$$

with

$$V_\lambda(r) = \int d\boldsymbol{r}_p \int d\boldsymbol{r}_T \rho_n(r_p)\rho_{T\lambda}(r_T)V_{NN}(\boldsymbol{r}-\boldsymbol{r}_p+\boldsymbol{r}_T). \quad (9)$$

In the isocentrifugal approximation, one then sets $\hat{\boldsymbol{r}}_d = 0$ and finally obtains [22]

$$V_{^{15}\mathrm{C}-T}(r,\theta) = \sum_\lambda V_\lambda(r)Y_{\lambda 0}(\theta). \quad (10)$$

We assume that the projectile nucleus ^{15}C takes the two-body structure, with the spherical core nucleus ^{14}C and a valence neutron. The density of the projectile is then given as

$$\rho_p(\boldsymbol{r}) = \rho_c(r) + \rho_n(r), \quad (11)$$

where $\rho_c(r)$ and $\rho_n(r)$ are the density for the core nucleus and the valence neutron, respectively. If one uses this density, the folding potential of Eq. (3) is also separated into two parts:

$$V_{^{15}\mathrm{C}-T}(r,\theta) = V_{^{14}\mathrm{C}-T}(r,\theta) + V_{n-T}(r,\theta). \quad (12)$$

For simplicity, we replace the interaction between the core and the target nuclei, $V_{^{14}\mathrm{C}-T}(r,\theta)$, by the deformed Woods-Saxon potential determined in the previous section.

For the density for the valence neutron, we construct it using a $2s_{1/2}$ neutron wave function in a Woods-Saxon potential as

$$\rho_n(r) = \frac{1}{4\pi}\left[R_{2s_{1/2}}(r)\right]^2, \quad (13)$$

where $R_{2s_{1/2}}(r)$ is the radial part of the wave function. To this end, we use the Woods-Saxon potential with set C in Ref. [37], which reproduces the empirical neutron separation energy for this state, $\epsilon_{2s_{1/2}} = -1.21$ MeV. Figure 2 shows the projectile density thus obtained. The blue dashed line shows the density for the core nucleus, ^{14}C, while the red dot-dashed line denotes the valence neutron density. For the description of the core density, we use the modified harmonic-oscillator model, whose parameters can be found in Ref. [35]. One can
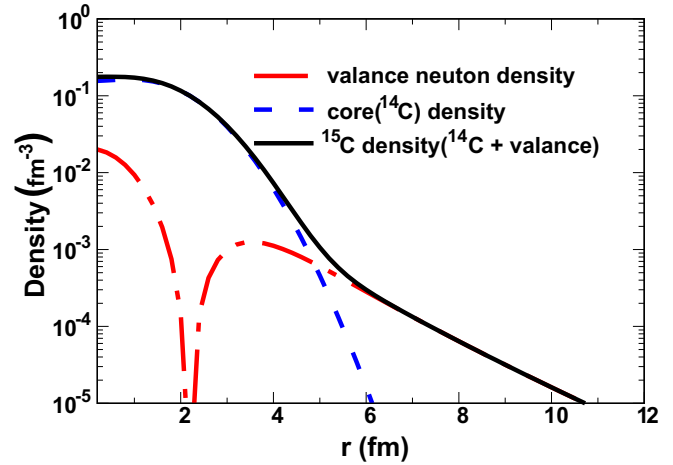

FIG. 2. The density distribution of the ^{15}C nucleus (the solid line). The dashed and the dot-dashed lines denote the contributions of the core nucleus and the valence neutron, respectively.

see that the valence neutron density has a long tail, reflecting the halo structure of the ^{15}C nucleus.

The solid lines in Fig. 3 shows the neutron-target potential obtained with the double folding procedure. The top, the middle, and the bottom panels show the monopole, the quadrupole, and the hexadecapole components, respectively. In order to discuss properties of these potentials, we fit them with a Woods-Saxon function and its first derivative. That is,

$$V_\lambda(r) = \frac{-V_0}{1 + \exp\left[(r-R_0)/a\right]} \quad (\lambda = 0), \quad (14)$$

$$= \frac{-V_0 \exp\left[(r-R_0)/a\right]}{\{1 + \exp\left[(r-R_0)/a\right]\}^2} \quad (\lambda = 2,4), \quad (15)$$

The results of the fitting are shown in Fig. 3 by the dashed lines (see Table II for the parameters). Since the region around the position of the Coulomb barrier is most important for fusion cross sections, the fittings are performed mainly in the surface region, $r > 8$ fm. In Fig. 3, one can see that the folding potential can be well fitted with the Woods-Saxon function. The hexadecapole component, $V_4(r)$, has some deviation from the Woods-Saxon function, but its contribution to the total potential is much smaller than the monopole and the quadrupole components. We also find that the contribution of $\lambda = 6$, that is, $V_6(r)$, is negligible, with a small depth size of about -0.1 MeV. Note that the Coulomb barrier parameters,

TABLE II. Parameters for the neutron-target part of the nuclear potential for the ^{15}C + ^{232}Th system. Those are obtained by fitting the double folding potential to the Woods-Saxon function and its derivative. The depth V_0, the radius R_0, and the diffuseness a parameters are shown for each multipole component.

V_λ	V_0 (MeV)	R_0 (fm)	a (fm)
$V_0(r)$	105.923	7.981	1.572
$V_2(r)$	28.756	7.080	1.890
$V_4(r)$	4.398	8.131	1.944

FIG. 4. The total potentials (the sum of the nuclear and the Coulomb potentials) for the ^{14}C + ^{232}Th and ^{15}C + ^{232}Th systems for $\theta = 0°$ and $\theta = 90°$. The solid and the dotted lines are for the ^{15}C + ^{232}Th system, for which the solid line corresponds to $\theta = 0°$ and the dashed line corresponds to $\theta = 90°$. The dashed and the dot-dashed lines are the same as the solid and the dotted lines, but for the ^{14}C + ^{232}Th system.

height is lowered by 1.53 MeV owing to the weakly bound valence neutron in ^{15}C.

Figure 4 shows the total potential (that is, the sum of the nuclear and the Coulomb potentials). The red dashed and the green dot-dashed lines show the potentials for the ^{14}C + ^{232}Th reaction at $\theta = 0°$ and at $\theta = 90°$, respectively. Note that the case of $\theta = 0°$ is referred to as a tip collision while that of $\theta = 90°$ is referred to as a side collision. The black solid and the blue dotted lines show the corresponding potentials for the ^{15}C + ^{232}Th reaction, obtained with the Woods-Saxon fit to the double folding potential between the valence neutron and the core nucleus. For both the cases, the Coulomb barrier is significantly lowered due to the addition of the valence neutron in ^{15}C. It is well known that lowering of the Coulomb barrier leads to an increase of the penetration probability for fusion cross sections.

B. Fusion cross sections

Let us now calculate fusion cross sections for the ^{15}C + ^{232}Th system using the potential constructed in the previous subsection. For simplicity, we include up to $\lambda = 4$ in the multipole expansion of the double folding potential between the valence neutron in ^{15}C and the target nucleus.

Figure 5 presents a comparison between the calculated fusion cross sections and the experimental data. The red circles and the blue stars show the experimental data for the ^{15}C + ^{232}Th and ^{14}C + ^{232}Th systems, respectively. The violet dashed curve shows the results for the ^{14}C + ^{232}Th system, which is the same as the solid line in Fig. 1. The coral dot-dashed curve shows the results for the ^{15}C + ^{232}Th system, obtained using the potential which is simply scaled from that for the ^{14}C + ^{232}Th system. That is, the radius parameter in the Woods-Saxon potential for the ^{14}C + ^{232}Th system is changed from $r_0(14^{1/3} + 232^{1/3})$ to $r_0(15^{1/3} + 232^{1/3})$. This

FIG. 3. The potential between the valence neutron in ^{15}C and the target nucleus ^{232}Th for the ^{15}C + ^{232}Th reaction. The top, the middle, and the bottom panels are for $V_0(r)$, $V_2(r)$, and $V_4(r)$ in Eq. (9), respectively. The black solid lines show the results of the double folding potential, while the red dashed lines show fits with the Woods-Saxon function.

obtained by setting the deformation parameters $\beta_{T\lambda}$ to be zero in the folding procedure, are $V_b = 58.81$ MeV, $R_b = 12.33$ fm, and $\hbar\Omega = 4.10$ MeV, which can be compared to those for the ^{14}C + ^{232}Th system listed in Table I. The Coulomb barrier

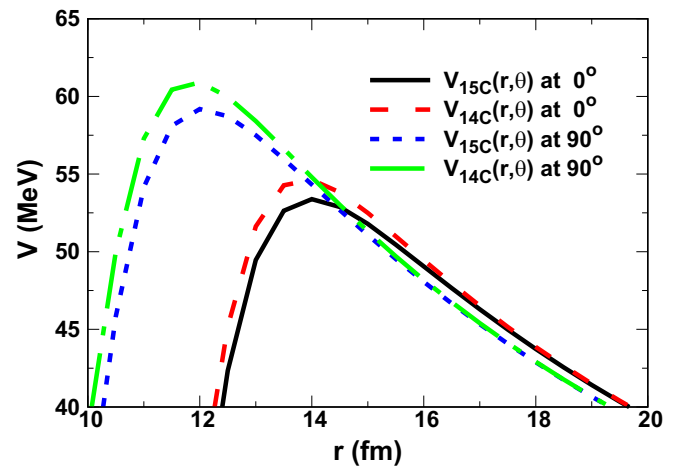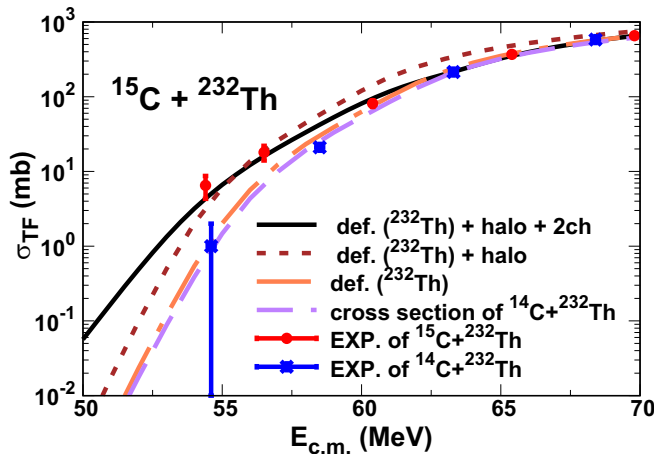FIG. 5. Fusion cross sections for the ^{15}C + ^{232}Th system. The dot-dashed line shows fusion cross sections obtained by scaling the potential for the ^{14}C + ^{232}Th system with the mass number of the colliding nuclei. The dotted line shows fusion cross sections with the double folding potential, which takes into account the halo structure of the ^{15}C nucleus, while the solid line shows the result of the coupled-channels calculation with the transfer coupling. For comparison, the figure also shows the theoretical fusion cross sections for the ^{14}C + ^{232}Th system by the dashed line. The experimental data are taken from Ref. [30].

calculation does not take into account the weakly bound nature of the ^{15}C projectile, and corresponds to the calculation presented in Ref. [30]. In fact, the dashed and dot-dashed lines show similar fusion cross sections to each other, as argued in Ref. [30]. Even though this calculation reproduces the experimental data at energies above the Coulomb barrier, $E_{c.m.} \gtrsim 60$ MeV, it considerably underestimates fusion cross sections in the energy region below the Coulomb barrier.

Fusion cross sections evaluated with the halo nature of the ^{15}C nucleus are shown by the brown dotted line. This result clearly shows an enhancement of fusion cross sections with respect to the dot-dashed line, and reproduces the experimental data at the two lowest energies. However, the fusion cross sections in the region of 60 MeV $\lesssim E_{c.m.} \lesssim 65$ MeV are clearly overestimated.

In order to investigate a possible origin for the discrepancy, we follow Ref. [18] and consider a transfer coupling to the ^{14}C + ^{233}Th channel. That is, we consider a transfer to a single effective channel [38] and solve the coupled-channels equations [22,31] of

$$\begin{pmatrix} K + V_1(r,\theta) & F_{1 \to 2}(r) \\ F_{1 \to 2}(r) & K + V_2(r,\theta) - Q \end{pmatrix} \begin{pmatrix} \psi_1(r) \\ \psi_2(r) \end{pmatrix} = E \begin{pmatrix} \psi_1(r) \\ \psi_2(r) \end{pmatrix}. \quad (16)$$

Here, the channels 1 and 2 denote the ^{15}C + ^{232}Th and the ^{14}C + ^{233}Th systems, respectively. K is the kinetic energy (with the centrifugal potential) and $V_i(r,\theta)$ ($i = 1, 2$) is the internucleus potential for each partition. Q is the effective Q value for the one-neutron transfer process, while $F_{1 \to 2}(r)$ is the coupling form factor. Notice that the effective transfer

TABLE III. The parameters for the transfer coupling. Here, those in the coupling form factor, Eq. (17), are determined by fitting the results of the coupled-channels calculations to the experimental fusion cross section for the ^{15}C + ^{232}Th system with $Q = 0$ for the transfer Q value.

Q (MeV)	F_t (MeV fm)	R_{coup} (fm)	a_{coup} (fm)
0	27.5	14.638	0.69

channel may mock up also the breakup channel to some extent.

In the calculation, we assume that the potential $V_2(r, \theta)$ for the ^{14}C + ^{233}Th channel is the same as the potential for ^{14}C + ^{232}Th presented in Table I. For the coupling form factor, $F_{1 \to 2}(r)$, we employ the derivative form of the Woods-Saxon potential [39,40] given by

$$F_{1 \to 2}(r) = F_t \frac{d}{dr} \left(\frac{1}{1 + \exp[(r - R_{coup})/a_{coup}]} \right). \quad (17)$$

The parameters are determined by fitting to the experimental data for fusion cross sections (see Table III). To this end, we take the transfer Q value to be zero, $Q = 0$, rather than the ground-state-to-ground-state Q value, $Q_{gg} = +3.568$ MeV, taking into account the Q-value matching condition [38]. The black solid line in Fig. 5 shows the fusion cross sections so obtained. One can see that the experimental data are well reproduced in the whole energy region shown in the figure, indicating an importance of the dynamical effect on fusion of the neutron-rich nucleus, ^{15}C.

IV. SUMMARY

We have calculated fusion cross sections for the ^{15}C + ^{232}Th system, for which ^{15}C is a well-known one-neutron halo nucleus while ^{232}Th is a well-deformed nucleus. To this end, we have evaluated the cross sections within the double folding formalism, taking into account the halo structure of ^{15}C and the deformation of the target nucleus. In addition, we have also taken into account the coupling to the one-neutron transfer channel to the ^{14}C + ^{233}Th system with the coupled-channels formalism. We have shown that such calculation reproduces simultaneously well the experimental data for the ^{15}C + ^{232}Th and ^{14}C + ^{232}Th systems. This clearly indicates that all of the halo structure of ^{15}C, the deformation of ^{232}Th, and the dynamical effects such as transfer and breakup play an important role in fusion of the ^{15}C + ^{232}Th system. In this regard, it would be useful to investigate systematically fusion of a halo nucleus with deformed target nuclei in order to gain a deeper insight into the role of deformation of the target in fusion of neutron-rich nuclei. A comparison of the ^{15}C + ^{232}Th system to the ^{15}C + ^{238}U and ^{15}C + ^{208}Pb systems might also provide useful information.

[1] P. Hansen and B. Jonson, Europhys. Lett. **4**, 409 (1987).

[2] I. Tanihata, H. Hamagaki, O. Hashimoto, Y. Shida, N. Yoshikawa, K. Sugimoto, O. Yamakawa, T. Kobayashi, and N. Takahashi, Phys. Rev. Lett. **55**, 2676 (1985).

[3] I. Tanihata, H. Hamagaki, O. Hashimoto, S. Nagamiya, Y. Shida, N. Yoshikawa, O. Yamakawa, K. Sugimoto, T. Kobayashi, D. Greiner, N. Takahashi, and Y. Nojiri, Phys. Lett. B **160**, 380 (1985).

[4] D. Bazin, W. Benenson, B. A. Brown, J. Brown, B. Davids, M. Fauerbach, P. G. Hansen, P. Mantica, D. J. Morrissey, C. F. Powell, B. M. Sherrill, and M. Steiner, Phys. Rev. C **57**, 2156 (1998).

[5] T. Nakamura, N. Fukuda, T. Kobayashi, N. Aoi, H. Iwasaki, T. Kubo, A. Mengoni, M. Notani, H. Otsu, H. Sakurai, S. Shimoura, T. Teranishi, Y. X. Watanabe, K. Yoneda, and M. Ishihara, Phys. Rev. Lett. **83**, 1112 (1999).

[6] K. Tanaka, T. Yamaguchi, T. Suzuki, T. Ohtsubo, M. Fukuda, D. Nishimura, M. Takechi, K. Ogata, A. Ozawa, T. Izumikawa, T. Aiba, N. Aoi, H. Baba, Y. Hashizume, K. Inafuku, N. Iwasa, K. Kobayashi, M. Komuro, Y. Kondo, T. Kubo *et al.*, Phys. Rev. Lett. **104**, 062701 (2010).

[7] T. Nakamura, N. Kobayashi, Y. Kondo, Y. Satou, N. Aoi, H. Baba, S. Deguchi, N. Fukuda, J. Gibelin, N. Inabe, M. Ishihara, D. Kameda, Y. Kawada, T. Kubo, K. Kusaka, A. Mengoni, T. Motobayashi, T. Ohnishi, M. Ohtake *et al.*, Phys. Rev. Lett. **103**, 262501 (2009).

[8] N. Kobayashi, T. Nakamura, Y. Kondo, J. A. Tostevin, Y. Utsuno, N. Aoi, H. Baba, R. Barthelemy, M. A. Famiano, N. Fukuda, N. Inabe, M. Ishihara, R. Kanungo, S. Kim, T. Kubo, G. S. Lee, H. S. Lee, M. Matsushita, T. Motobayashi, T. Ohnishi *et al.*, Phys. Rev. Lett. **112**, 242501 (2014).

[9] N. Takigawa and H. Sagawa, Phys. Lett. B **265**, 23 (1991).

[10] N. Takigawa, M. Kuratani, and H. Sagawa, Phys. Rev. C **47**, R2470(R) (1993).

[11] M. S. Hussein, M. P. Pato, L. F. Canto, and R. Donangelo, Phys. Rev. C **47**, 2398 (1993).

[12] C. H. Dasso and A. Vitturi, Phys. Rev. C **50**, R12(R) (1994).

[13] K. Hagino, A. Vitturi, C. H. Dasso, and S. M. Lenzi, Phys. Rev. C **61**, 037602 (2000).

[14] A. Diaz-Torres and I. J. Thompson, Phys. Rev. C **65**, 024606 (2002).

[15] M. Ito, K. Yabana, T. Nakatsukasa, and M. Ueda, Phys. Lett. B **637**, 53 (2006).

[16] L. Canto, P. Gomes, R. Donangelo, and M. Hussein, Phys. Rep. **424**, 1 (2006).

[17] L. Canto, P. Gomes, R. Donangelo, J. Lubian, and M. Hussein, Phys. Rep. **596**, 1 (2015).

[18] K.-S. Choi, M.-K. Cheoun, W. Y. So, K. Hagino, and K. S. Kim, Phys. Lett. B **780**, 455 (2018).

[19] K.-S. Choi, M.-K. Cheoun, K. S. Kim, T. Kim, and W. Y. So, J. Korean Phys. Soc. **70**, 42 (2017).

[20] A. B. Balantekin and N. Takigawa, Rev. Mod. Phys. **70**, 77 (1998).

[21] M. Dasgupta, D. J. Hinde, N. Rowley, and A. M. Stefanini, Annu. Rev. Nucl. Part. Sci. **48**, 401 (1998).

[22] K. Hagino and N. Takigawa, Prog. Theor. Phys. **128**, 1061 (2012).

[23] B. B. Back, H. Esbensen, C. L. Jiang, and K. E. Rehm, Rev. Mod. Phys. **86**, 317 (2014).

[24] G. Montagnoli and A. M. Stefanini, Eur. Phys. J. A **53**, 169 (2017).

[25] A. M. Vinodkumar, W. Loveland, R. Yanez, M. Leonard, L. Yao, P. Bricault, M. Dombsky, P. Kunz, J. Lassen, A. C. Morton, D. Ottewell, D. Preddy, and M. Trinczek, Phys. Rev. C **87**, 044603 (2013).

[26] R. Raabe, J. Sida, J. Charvet, N. Alamanos, C. Angulo, J. Casandjian, S. Courtin, A. Drouart, D. Durand, P. Figuera *et al.*, Nature (London) **431**, 823 (2004).

[27] A. Hassan *et al.*, Bull. Russ. Acad. Sci. Phys **70**, 1558 (2006).

[28] J. J. Kolata, V. Guimarães, D. Peterson, P. Santi, R. White-Stevens, P. A. DeYoung, G. F. Peaslee, B. Hughey, B. Atalla, M. Kern, P. L. Jolivette, J. A. Zimmerman, M. Y. Lee, F. D. Becchetti, E. F. Aguilera, E. Martinez-Quiroz, and J. D. Hinnefeld, Phys. Rev. Lett. **81**, 4580 (1998).

[29] C. Signorini, A. Yoshida, Y. Watanabe, D. Pierroutsakou, L. Stroe, T. Fukuda, M. Mazzocco, N. Fukuda, Y. Mizoi, M. Ishihara, H. Sakurai, A. Diaz-Torres, and K. Hagino, Nucl. Phys. A **735**, 329 (2004).

[30] M. Alcorta, K. E. Rehm, B. B. Back, S. Bedoor, P. F. Bertone, C. M. Deibel, B. DiGiovine, H. Esbensen, J. P. Greene, C. R. Hoffman, C. L. Jiang, J. C. Lighthall, S. T. Marley, R. C. Pardo, M. Paul, A. M. Rogers, C. Ugalde, and A. H. Wuosmaa, Phys. Rev. Lett. **106**, 172701 (2011).

[31] K. Hagino, N. Rowley, and A. T. Kruppa, Comput. Phys. Commun. **123**, 143 (1999).

[32] K. Hagino, Phys. Rev. C **98**, 014607 (2018).

[33] Ö. Akyüz and A. Winther, in *Nuclear Structure and Heavy-Ion Collisions*, Proceedings of the International School of Physics "Enrico Fermi," Course 77, Varenna, 1979 (North-Holland, Amsterdam, 1981).

[34] J. Zumbro, R. Naumann, M. Hoehn, W. Reuter, E. Shera, C. Bemis, and Y. Tanaka, Phys. Lett. B **167**, 383 (1986).

[35] H. D. Vries, C. D. Jager, and C. D. Vries, At. Data Nucl. Data Tables **36**, 495 (1987).

[36] G. Bertsch, J. Borysowicz, H. McManus, and W. Love, Nucl. Phys. A **284**, 399 (1977).

[37] K. Hagino and H. Sagawa, Phys. Rev. C **75**, 021301(R) (2007).

[38] N. Rowley, in *Proceedings of the International Workshop on Fusion Dynamics at the Extremes*, edited by by Y. Ts. Oganessian and V. I. Zagrebaev (World Scientific, Singapore, 2001), p. 296.

[39] C. H. Dasso and A. Vitturi, Phys. Lett. B **179**, 337 (1986).

[40] C. Dasso and G. Pollarolo, Phys. Lett. B **155**, 223 (1985).